

One Network to Solve All ROIs: Deep Learning CT for Any ROI using Differentiated Backprojection

Yoseob Han, and Jong Chul Ye*

Bio Imaging, Signal Processing, and Learning Group

Dept. of Bio and Brain Engineering, KAIST

Daejeon, Republic of Korea

**Corresponding author: jong.ye@kaist.ac.kr*

Purpose: Computed tomography for region-of-interest (ROI) reconstruction has advantages of reducing X-ray radiation dose and using a small detector. However, standard analytic reconstruction methods suffer from severe cupping artifacts, and existing model-based iterative reconstruction methods require extensive computations. Recently, we proposed a deep neural network to learn the cupping artifact, but the network is not well generalized for different ROIs due to the singularities in the corrupted images. Therefore, there is an increasing demand for a neural network that works well for any ROI sizes.

Method: Two types of neural networks are designed. The first type learns ROI size-specific cupping artifacts from the analytic reconstruction images, whereas the second type network is to learn to invert the finite Hilbert transform from the truncated differentiated backprojection (DBP) data. Their generalizability for any ROI sizes is then examined.

Results: Experimental results show that the new type of neural network significantly outperforms the existing iterative methods for any ROI sizes in spite of significantly reduced run-time complexity.

Conclusions: Since the proposed method consistently surpasses existing methods for any ROIs, it can be used as a general CT reconstruction engine for many practical applications without compromising possible detector truncation.

I. INTRODUCTION

X-ray Computed Tomography (CT) is one of the most powerful clinical imaging tools, delivering high-quality images in a fast and cost effective manner. However, X-ray radiation from CT increases the potential risk of cancers to patients, so many studies has been conducted to reduce the X-ray dose. In particular, low dose X-ray CT technology has been extensively developed by reducing the number of photons, projection views, or ROI sizes. Among these, the interior tomography aims to obtain an ROI image by irradiating only within the ROI. Interior tomography is useful when the ROI within a patient's body is small (such as heart). In some applications, interior tomography has additional benefits thanks to the cost saving from using a small-sized detector. However, the use of an analytic CT reconstruction algorithm generally produces images with severe cupping artifacts due to the transverse directional projection truncation.

Sinogram extrapolation is a simple but inaccurate approximation method to reduce the artifacts¹. Recently, it has been shown that an ROI image can be reconstructed uniquely from truncated projection data when the intensity of the subregions inside the ROI are known *a priori*². Assuming some prior knowledges of the functional space for images, Katsevich et al³ proved the general uniqueness results for the interior problem and provided stability estimates. In Jin et al⁴, a continuous domain singular value decomposition of the finite Hilbert transform operator characterized in Katsevich et al⁵ was used to represent an interior image with a linear combination of the eigen-functions, after which the null space compensation was performed by using a more general set of prior subregion knowledge. Using the total variation (TV) penalty, Yu et al⁶ showed that a unique reconstruction is possible if the images are piecewise smooth. In a series of papers^{7,8}, our group has also shown that a generalized L-spline along a collection of chord lines passing through the ROI can be uniquely recovered⁷; and we have further confirmed that the high frequency signal can be analytically recovered thanks to the Bedrosian identity, whereas the computationally intensive iterative reconstruction only need to be performed to reconstruct the low frequency part of the signal after downsampling⁸. While this approach significantly reduces the computational complexity of the interior reconstruction, the computational complexity of this technique, as well as most existing iterative reconstruction algorithms, still prohibits their routine clinical use.

In recent years, deep learning algorithms using convolutional neural network (CNN) has made remarkable success in various applications⁹⁻¹⁴. In particular, various deep learning architecture have been successfully used for low-dose CT^{11,12,15}, sparse view CT^{13,14,16}, etc. These deep learning applications surpassed the previous iterative methods in image quality and reconstruction time. Moreover, in a recent theory of deep convolutional framelets¹⁷, the authors showed that the success of deep learning comes from the power of a novel signal representation using non-local basis combined with data-driven local basis. Thus, the deep network is indeed a natural extension of classical signal representation theory such as wavelets, frames, etc, which is useful for inverse problems.

Inspired by these findings, here we propose deep learning frameworks for interior tomography problem. One of the most important contributions of this paper is the observation that there are two ways of addressing the interior tomography that can be directly translated into two distinct neural network architectures. More specifically, it is well-known that the technical difficulties of interior tomography arises from the existence of the null space in the finite Hilbert transform⁵. One way to address this difficulty is a post-processing approach to remove the null space image from the analytic reconstruction. In fact, our preliminary work¹⁸ is the realization of such idea in neural network domain, which was trained to learn the cupping artifacts corresponding to the null space images. On the other hand, a direct inversion can be done from the truncated DBP data using an inversion formula for finite Hilbert transform¹⁹. While this approach has been investigated by several pioneering works for interior tomography problems²⁰, the main limitation of these approaches is that the inversion formula is not unique due to the existence of null-space, but the selection of the optimal parameter for the null-space image to ensure the uniqueness is intractable. Another novel contribution of this work is the second type of neural network that is designed to learn to invert the finite Hilbert transform from the truncated DBP data by learning the null space parameters and convolutional kernel for Hilbert transform from the training data.

Although the two neural network approaches appear similar except their inputs, there are fundamental differences in their generalization capability. The first type network learns the null-space components from the artifacts corrupted input images. Although the approach provides near-perfect reconstruction with about 7 ~ 10dB improvement in PSNR over existing methods¹⁸, the null-space component of the analytic reconstruction contains the singularity at the ROI boundary with strong intensity saturation, so the trained net-

work for particular ROI size does not generalize well for different ROI sizes. On the other hand, the input image for the second type network is the truncated DBP images, which corresponds to the full DBP images on an ROI mask. Therefore, there are no singularities in the DBP images, which generalizes the network for different ROI sizes. Numerical results showed that while the second thype network outperforms the existing interior tomography techniques for all ROIs in terms of image quality and reconstruction time, the first type network degrades rapidly if the ROI size differs from the training data.

This paper is structured as follows. In Section II, the basic theory of differentiated backprojection (DBP) and Hilbert transform are reviewed, the interior tomography problem is formally defined, from which two types of neural network architectures are derived. Then, Section III describes the methods to implement and validate the proposed method, which is followed by experimental results in Section IV. Conclusions are provided in Section V.

II. THEORY

For simplicity, we consider 2-D interior tomography problem throughout the paper, but the extension to 3-D problem is straightforward.

II.A. Differentiated Backprojection and Hilbert Transform

The variable $\boldsymbol{\theta}$ denotes a vector on the unit sphere $\mathbb{S} \in \mathbb{R}^2$. The collection of vectors that are orthogonal to $\boldsymbol{\theta}$ is denoted as

$$\boldsymbol{\theta}^\perp = \{\mathbf{y} \in \mathbb{R}^2 : \mathbf{y} \cdot \boldsymbol{\theta} = 0\}.$$

We refer to real-valued functions in the spatial domain as images and denote them as $f(\mathbf{x})$ for $\mathbf{x} \in \mathbb{R}^2$. We denote the Radon transform of an image f as

$$\mathcal{R}f(\boldsymbol{\theta}, s) := \int_{\boldsymbol{\theta}^\perp} f(s\boldsymbol{\theta} + \mathbf{y})d\mathbf{y} \tag{1}$$

where $s \in \mathbb{R}$ and $\boldsymbol{\theta} \in \mathbb{S}$. We further define the X-ray transform D_f that maps a function on \mathbb{R}^2 into the set of its line integrals:

$$D_f(\mathbf{a}, \boldsymbol{\theta}) = \int_0^\infty dt f(\mathbf{a} + t\boldsymbol{\theta}) , \tag{2}$$

where $\mathbf{a} \in \mathbb{R}^2$ refer to the X-ray source location. For a given object function $f(\mathbf{x})$ and a given source trajectory $\mathbf{a}(\lambda), \lambda \in [\lambda_{\min}, \lambda_{\max}]$, the differentiated backprojection (DBP) is then computed by²¹⁻²³:

$$g(\mathbf{x}) = \int_{\lambda^-}^{\lambda^+} d\lambda \frac{1}{\|\mathbf{x} - \mathbf{a}(\lambda)\|} \left. \frac{\partial}{\partial \mu} D_f(\mathbf{a}(\mu), \boldsymbol{\theta}) \right|_{\mu=\lambda} \quad (3)$$

where $[\lambda^-, \lambda^+] \subset [\lambda_{\min}, \lambda_{\max}]$ denotes the appropriate intervals from the source segments between λ_{\min} and λ_{\max} , and $1/\|\mathbf{x} - \mathbf{a}(\lambda)\|$ denotes the distance weighting.

One of the most important aspects of the DBP formula in (3) is its relation to the analytic reconstruction methods. More specifically, let the source trajectory $\mathbf{a}(\lambda), \lambda \in [\lambda^-, \lambda^+]$ have no discontinuities. Suppose, furthermore, \mathbf{x} is on the connecting line of the two source positions $\mathbf{a}(\lambda^-)$ and $\mathbf{a}(\lambda^+)$. Then, the differentiated backprojection data in (3) can be represented as²¹⁻²³:

$$g(\mathbf{x}) = \frac{1}{(2\pi)^2} \int d\boldsymbol{\omega} \hat{f}(\boldsymbol{\omega}) e^{j\mathbf{x} \cdot \boldsymbol{\omega}} j\sigma(\mathbf{x}, \boldsymbol{\omega}, \lambda^-, \lambda^+) \quad (4)$$

where

$$\sigma(\mathbf{x}, \boldsymbol{\omega}, \lambda^-, \lambda^+) = \frac{1}{2} [\text{sgn}(\boldsymbol{\alpha}(\lambda^-, \mathbf{x}) \cdot \boldsymbol{\omega}) - \text{sgn}(\boldsymbol{\alpha}(\lambda^+, \mathbf{x}) \cdot \boldsymbol{\omega})], \quad (5)$$

$$\boldsymbol{\alpha}(\lambda, \mathbf{x}) = \frac{\mathbf{x} - \mathbf{a}(\lambda)}{\|\mathbf{x} - \mathbf{a}(\lambda)\|}.$$

and $\text{sgn}(\cdot)$ denotes the signum function.

The connecting line between the two sources position is often called a *chord line*²¹⁻²³. If the unit vector \mathbf{e} along the chord line is set as a coordinate axis, then we can find the orthonormal basis \mathbf{e}^\perp such that $V = [\mathbf{e}, \mathbf{e}^\perp]$ consists of the basis for the local coordinate system at $\mathbf{a}(\lambda^-)$ (see Fig. 1). Suppose $(u, v) \in \mathbb{R}^2$ denotes the coordinate value on the new coordinate system composed of \mathbf{e} and \mathbf{e}^\perp . Then, the authors in²¹⁻²³ showed that (4) can be converted into the following form:

$$g_v(u) = \int \frac{d\eta}{\pi(u - \eta)} f_v(\eta) := \mathcal{H}f_v(u) \quad (6)$$

where $g_v(u)$ and $f_v(u)$ denote the restriction of $g(\mathbf{x})$ and $f(\mathbf{x})$ on the chord line index v , respectively; and \mathcal{H} denotes the Hilbert transform along the chord line. Because $\mathcal{H}\mathcal{H} = -I$, we have

$$f_v(u) = -\mathcal{H}g_v(u), \quad (7)$$

which is known as the backprojection filtration (BPF) method that recovers the object on each chord line by taking the Hilbert transform of the DBP data²¹⁻²³.

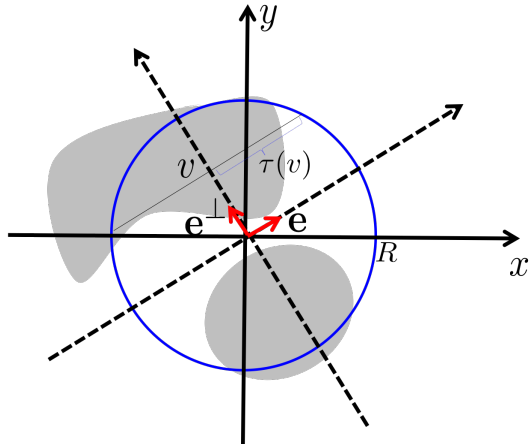


FIG. 1 The coordinate system for interior tomography.

II.B. Problem Formulation

The measurement of the interior tomography problem is the restriction of the radon measurement $\mathcal{R}f$ to the region $\{(\boldsymbol{\theta}, s) : |s| < R\}$, where R denotes the radius of the ROI. In the DBP domain, this is equivalent to find the unknown $f_v(u), |u| < \tau$ on the chord line indexed by v using the DBP measurement $g_v(u), |u| < \tau$, where $\tau := \tau(v)$ denotes the chord line dependent 1-D restriction of the ROI (see Fig. 1).

More specifically, let \mathcal{I}_τ be the indicator function between $[-\tau, \tau]$:

$$\mathcal{I}_\tau g(u) = \begin{cases} g(u), & |u| \leq \tau \\ 0, & \text{otherwise} \end{cases}.$$

We further define the truncated Hilbert transform:

$$\mathcal{T}_\tau f(u) = \mathcal{I}_\tau \mathcal{H}f(u) = \int_{-\tau}^{\tau} \frac{f(u')}{\pi(u - u')} du'. \quad (8)$$

Then, the resulting 1-D interior tomography problem can be formally stated as

$$(P) : \text{Find } f_v(u) \text{ such that } \mathcal{I}_\tau g_v(u) = \mathcal{T}_\tau f_v(u) \quad (9)$$

In order to obtain 2-D image within the ROI, this problem should be solved for all $|v| < R$.

In the following, we denote with a slight abuse of notation $g(u) := g_v(u)$ and $f(u) := f_v(u)$, if there are no concerns about the potential confusion.

II.C. Inversion of Finite Hilbert Transform using Neural Networks

The main technical difficulty of the interior reconstruction (P) is the existence of the null space of the truncated Hilbert transform^{5,7}. More specifically, there exists the non-zero $f_{\mathcal{N}}(u)$ such that

$$\mathcal{T}_{\tau} f_{\mathcal{N}}(u) = 0, \quad |u| < \tau,$$

Indeed, $f_{\mathcal{N}}(x)$ can be expressed such that

$$f_{\mathcal{N}}(u) = -\frac{1}{\pi} \int_{\mathbb{R} \setminus [-\tau, \tau]} \frac{\psi(u')}{u - u'} du'. \quad (10)$$

for any function $\psi(u)$ outside of the ROI. A typical example of an 1-D null space image $f_{\mathcal{N}}$ for a given ψ is illustrated in Fig. 2(a) for the case of $\tau = 0.5$, where the null space signal contains the singularities at $u = \pm 0.5$. An example of 2-D image null space image is also shown in Fig. 2(b), in which the singularities also exists at the ROI boundary. These are often called as the cupping artifact because they are shaped like a cup with a stronger bias of CT number near the ROI boundary. The cupping artifacts reduce contrast and interfere with clinical diagnosis.

In the first type of neural network (type I neural network), which is a direction extension of our preliminary work¹⁸, a neural network \mathcal{Q} is designed such that

$$\mathcal{Q}(\mathbf{f} + \mathbf{f}_{\mathcal{N}}) = \mathbf{f} \quad (11)$$

where \mathbf{f} and $\mathbf{f}_{\mathcal{N}}$ denote the collection of 2-D ground-truth signal and its null-space images. For this network, the null space corrupted input images can be easily obtained by

$$\mathbf{f} + \mathbf{f}_{\mathcal{N}} = \mathcal{M}\mathbf{p},$$

where \mathcal{M} denotes an analytic inversion formula such as the filtered backprojection (FBP) algorithm, and \mathbf{p} denotes the zero-padded truncated projection data. See Fig. 3(a) for such network. Then, the neural network training problem can be performed as

$$\min_{\mathcal{Q}} \sum_{i=1}^N \|\mathbf{f}^{(i)} - \mathcal{Q}\mathcal{M}\mathbf{p}^{(i)}\|^2 \quad (12)$$

where $\{(\mathbf{f}^{(i)}, \mathbf{p}^{(i)})\}_{i=1}^N$ denotes the training data set composed of ground-truth image and its truncated projection. This method is simple to implement, and provides significant gain over the existing iterative methods¹⁸.

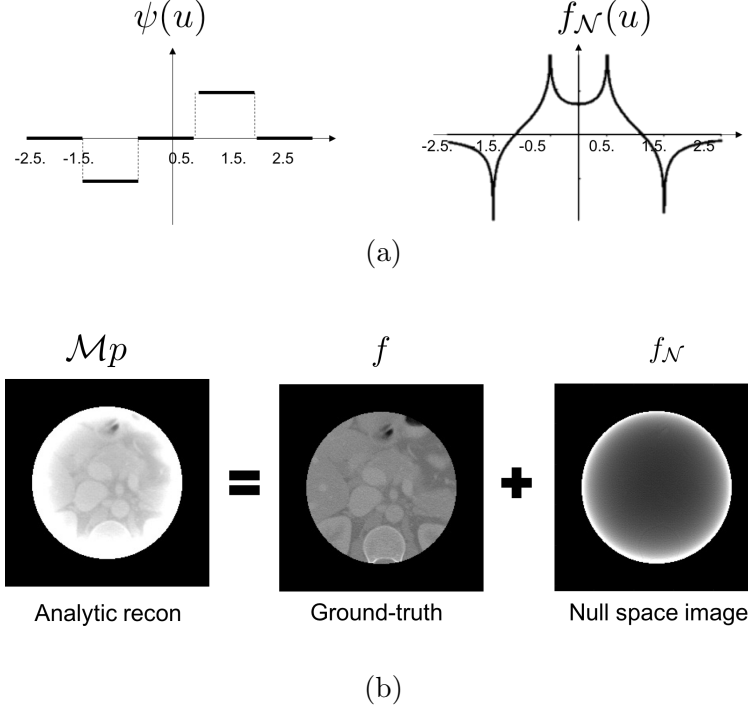


FIG. 2 (a) one-dimensional null space signal, and (b) 2-D null space image.

However, one of the main technical issues of this network architecture is that the input images is corrupted with the singularities from the null-space images at the ROI boundaries as shown in Fig. 2. Due to the strong intensity at the ROI boundaries, the network training is strongly dependent on ROI size-dependent cupping artifacts and the trained network does not generalize well as will be shown in experimental section. This would not be a problem when a specific ROI size is used for all interior tomography problems. However, in many practical applications such as interventional imaging, cardiac imaging, etc, the size of the ROI is mainly dependent on the subject size and clinical procedures, so there are many demands for flexible ROI sizes during the imaging. In this case, various neural network models for numerous ROI sizes should be stored, which is not practical.

To design such neural networks that generalizes well for all ROI sizes, let us revisit the truncated Hilbert transform (8). For simplicity, we now assume $\tau = 1$ and $\mathcal{T} := \mathcal{T}_1$. Then, the following formula is well-known as an inversion formula for the finite Hilbert transform¹⁹:

$$f(u) = \frac{c}{\sqrt{1-u^2}} - \frac{1}{\pi\sqrt{1-u^2}} \int_{-1}^1 \frac{\sqrt{1-s^2}g(s)}{u-s} ds \quad (13)$$

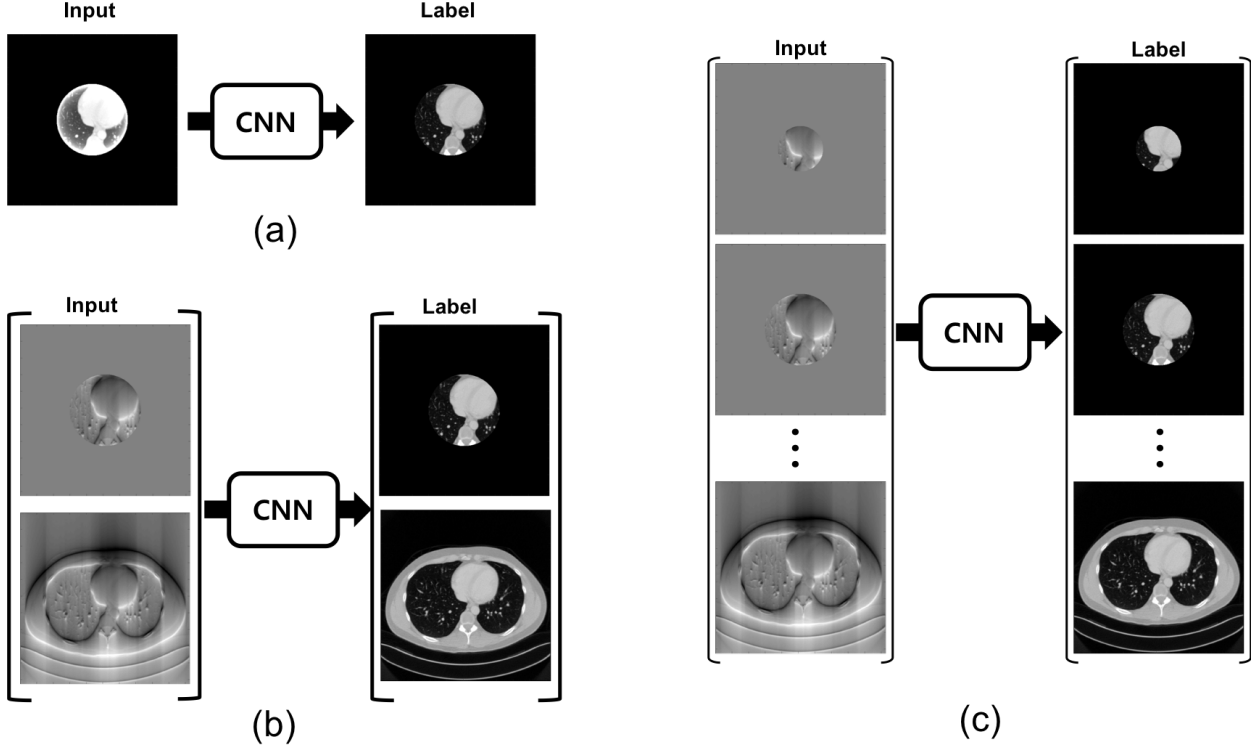


FIG. 3 Different training architecture for the interior tomography problems. (a) Type I network trained to learning the cupping artifacts from the analytic reconstruction, and type II networks trained to learn the inversion of the truncated Hankel transform, using truncated DBP data from (b) a 380 detectors, and (c) various detector sizes.

where the constant c is given by

$$c := \frac{1}{\pi} \int_{-1}^1 f(s) ds. \quad (14)$$

This formula has been used in some of the existing interior tomography approaches²⁰. Although the formula (13) with (14) appear the desired inversion formula for the finite Hilbert transform that can be directly used for interior tomography problems, the main weakness of this formula is that the expression is not unique. More specifically, the constant c is in fact arbitrary since $1/\sqrt{1-u^2}$ lives in the null space of the truncated Hilbert transform¹⁹:

$$\mathcal{T} \left(\frac{1}{\sqrt{1-u^2}} \right) = 0. \quad (15)$$

Thus, finding the optimal choice of c is not possible by only considering 1-D problem. In fact, the value c must be chosen by considering adjacent chord lines to make the final 2-D image realistic and free of line artifacts, which is however intractable and has not been attempted to our best understanding.

To investigate how this problem can be addressed using the second type of neural network (type II network), note that the inversion formula can be converted to

$$(w_\tau \odot f_v)(u) = c_v - h * (w_\tau \odot g)(u), \quad |v| < R \quad (16)$$

where $\tau := \tau(v)$ denotes the window size for the chord line index v , \odot denotes the element-wise product, and $w_\tau(u)$ is the analytic form of weighting given by

$$w_\tau(u) = \sqrt{\tau^2 - u^2}, \quad |u| \leq \tau,$$

and h is the convolution kernel for Hilbert transform, and c_v is the unknown constant. Since the analytic weighting w_τ can be readily calculated once the FOI size is detected from the truncated DBP input, the required parameters for the reconstruction of $(w_\tau \odot f_v)$ is the convolutional kernel h and the constant c_v for all chord line index $|v| < R$. Then, after the reconstruction, the weight w_τ can be removed and the final image f_v can be obtained for all $|v| < R$.

In fact, this algorithmic procedure can be readily learned using a deep neural network. Specifically, we construct a neural network \mathcal{S} such that

$$\mathbf{f} = \mathcal{S}\mathbf{g},$$

where \mathbf{g} denotes the truncated DBP data for all chord lines, and \mathbf{f} is the 2-D ground-truth image. In fact, the roles of the neural network \mathcal{S} are to estimate the ROI size R (and its restriction τ) from the truncated DBP input to calculate the weighting, and to learn the convolutional kernel for Hilbert transform as well as the constant c_v for all $|v| < R$.

Such neural network training problem can be performed as

$$\min_{\mathcal{S}} \sum_{i=1}^N \|\mathbf{f}^{(i)} - \mathcal{S}\mathbf{g}^{(i)}\|^2 \quad (17)$$

where $\{(\mathbf{f}^{(i)}, \mathbf{g}^{(i)})\}_{i=1}^N$ denotes the training data set composed of ground-truth image and its 2-D DBP data. Here it is important to note that the network could learn the reverse Hilbert transform for the full DBP data if no truncated DBP data is used during the training. Therefore, truncated DBP data and the corresponding truncated ground-truth image should be used as input and label data along with the non-truncated DBP data so that the network can learn to invert the finite Hilbert transform.

In contrast to the type I neural network \mathcal{Q} , the type II neural network \mathcal{S} has truncated DBP data as input, which are just ROI images of the full DBP data. So there exists no singularities in the input data. Later we will show that such a trained neural network has a significant generalization power so that it can be used for any ROI sizes.

III. METHOD

III.A. Data Set

Ten subject data sets from American Association of Physicists in Medicine (AAPM) Low-Dose CT Grand Challenge was used in this paper. The provided data sets were originally acquired in helical CT, and were rebinned from the helical CT to 360° angular scan fan-beam CT. The 512×512 size artifact-free CT images are reconstructed from the rebinned fan-beam CT data using filtered backprojection (FBP) algorithm. From the CT images, sinogram are numerically obtained using forward fan-beam projection operator for our experiments. The number of detector is 1440 elements with pitch of 1 mm. The number of views is 1200. The distance from source to rotation axis (DSO) is 800 mm and the distance from source to detector (DSD) is 1400 mm. Out of ten sets, eight sets were used for network training, one set was used for validation, and the other set was used for test. This corresponds to 3720, 254, and 486 slices of 512×512 size for training, validation, and test data, respectively.

Fig. 3(a) shows a flowchart of the training scheme for the type I neural network \mathcal{Q} that learns the artifact patterns in the analytic reconstruction images from the truncated projection data. In this case, the input image is corrupted with the cupping artifact, whereas the clean data with the same ROI is used as the ground truth. In this experiment, we used 380 detectors and the radius of the ROI was 107.59 mm, which is about 30% of the total ROI.

Fig. 3(b)(c) shows a flowchart of the training scheme for the type II neural networks \mathcal{S} that learn the inverse of the finite Hilbert transform. The truncated DBP data has no singularities regardless of the truncation ratio. In fact, the truncated DBP data are exactly the same as the full DBP data within the ROI mask. We trained two networks. One network was trained with only 380 detectors and full detectors (see Fig. 3(b)), whereas the other network is trained with various ROIs generated by 240, 380, 600, 1440 detectors (see Fig.

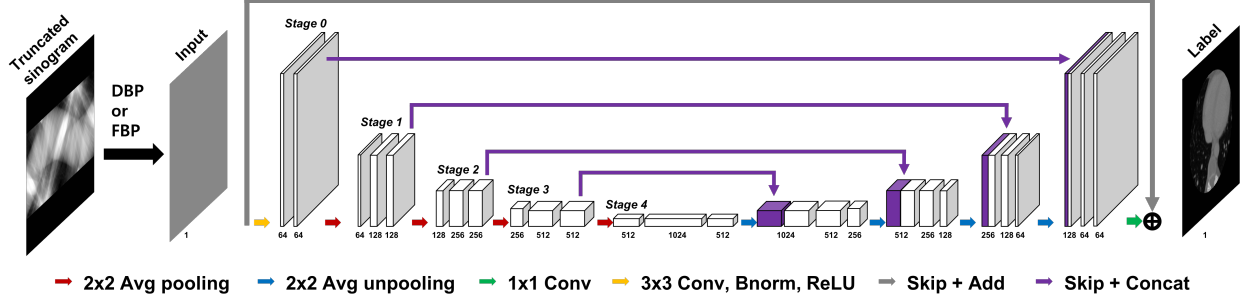


FIG. 4 The proposed deep learning architecture.

3(c)). This corresponds to the ratio of 19, 29, 46, and 100%, respectively.

It is important to note that the type I network in Fig. 3(a) cannot be trained with the complete projection data similar to the type II network in Fig. 3(b). This is because, in this case, the input and label data are both artifact-free FBP data, so that the neural network becomes identity mapping. This suggests another key benefit of the Type II network, which can use both truncated and full DBP data as input so that the network can be used not only for the interior problems but also for standard CT reconstruction.

For quantitative evaluation, we use the peak signal to noise ratio (PSNR), defined by

$$PSNR = 20 \cdot \log_{10} \left(\frac{nm \|f^*\|_{\infty}}{\|\hat{f} - f^*\|_2} \right), \quad (18)$$

where \hat{f} and f^* denote the reconstructed image and ground truth, respectively; m and n are the number of pixel for row and column. We also used the structural similarity (SSIM) index²⁴, defined as

$$SSIM = \frac{(2\mu_{\hat{f}}\mu_{f^*} + c_1)(2\sigma_{\hat{f}f^*} + c_2)}{(\mu_{\hat{f}}^2 + \mu_{f^*}^2 + c_1)(\sigma_{\hat{f}}^2 + \sigma_{f^*}^2 + c_2)}, \quad (19)$$

where $\mu_{\hat{f}}$ is a average of \hat{f} , $\sigma_{\hat{f}}^2$ is a variance of \hat{f} and $\sigma_{\hat{f}f^*}$ is a covariance of \hat{f} and f^* . There are two variables to stabilize the division such as $c_1 = (k_1L)^2$ and $c_2 = (k_2L)^2$. L is a dynamic range of the pixel intensities. k_1 and k_2 are constants by default $k_1 = 0.01$ and $k_2 = 0.03$. We also use the normalized mean square error (NMSE).

III.B. Network Architecture

The same network architecture shown in Fig. 4 is used for the type I and type II networks, in which only difference is from their input images. The type I network uses the FBP images

as input, while the type II network uses the DBP data. The network backbone corresponds to a modified architecture of U-Net¹⁰. A yellow arrow in Fig. 4 is the basic operator and consists of 3×3 convolutions followed by a rectified linear unit (ReLU) and batch normalization. The yellow arrows between the separate blocks at every stage are omitted. A red arrow is a 2×2 average pooling operator and located between the stages. Average pooling operator doubles the number of channels and reduces the size of the layers by four. In addition, a blue arrow is 2×2 average unpooling operator, reducing the number of channels by half and increasing the size of the layer by four. A violet arrow is the skip and concatenation operator. A green arrow is the simple 1×1 convolution operator generating final reconstruction image. Finally, a gray arrow is the skip and addition operator for residual learning.

III.C. Network training

The type I and type II networks were implemented using MatConvNet toolbox (ver.24) in MATLAB R2015a environment²⁵. Processing units used in this research are Intel Core i7-7700 (3.60GHz) central processing unit (CPU) and GTX 1080 Ti graphics processing unit (GPU). Stochastic gradient descent (SGD) method was used to train the network. The number of epochs was 300. The initial learning rate was 10^{-4} , which gradually dropped to 10^{-5} at each epoch. The regularization parameter was 10^{-4} . For data augmentation, input data was performed with horizontal and vertical flipping. In addition, mini-batch data was used, and the size of input patch is 256×256 . Since the trained convolution kernel has spatially invariant properties, these filters can be used for the entire input data in the inference phase. The size of entire input data is 512×512 . Training time lasted about 24 hours.

IV. EXPERIMENTAL RESULTS

Due to the null space image that has singularity in the ROI boundary, the type I network training with analytic reconstruction is quite dependent upon the input ROI size. Thus, we conjectured that the type I network with a specific ROI may not generalize well for other ROI sizes.

To confirm the performance degradation of type I network with respect to varying ROI

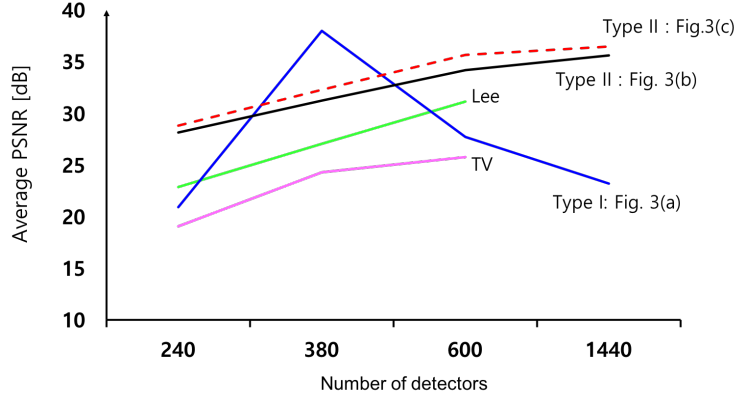


FIG. 5 Average PSNR values change with respect to the number of detectors.

TABLE I Quantitative comparison with respect to various detector sizes.

PSNR [dB]		TV	Lee ⁸	Type I (Fig. 3(a))	Type II (Fig. 3(b))	Type II (Fig. 3(c))
# of detector	240	19.0360	22.8487	20.9016	28.1598	28.8206
	380	24.2809	27.0543	38.0112	31.2188	32.2786
	600	25.7784	31.1304	27.7033	34.1692	35.6654
	1440	-	-	23.1952	35.6034	36.4700
SSIM		TV	Lee ⁸	Type I (Fig. 3(a))	Type II (Fig. 3(b))	Type II (Fig. 3(c))
# of detector	240	0.8657	0.9599	0.9262	0.9613	0.9658
	380	0.9161	0.9701	0.9917	0.9723	0.9758
	600	0.9289	0.9777	0.9608	0.9761	0.9804
	1440	-	-	0.9162	0.9345	0.9450

sizes, the trained network was applied to the test data with 240, 380, 600, and 1440 detectors. The average PSNR and SSIM values are described in the Table I. Since the type I network was trained with 380 detector data, it performed better than the type II network for the case of the 380 detector as shown in Fig. 5 and Table I. Type II network shows the highest values in PSNR and SSIM, except 380 detector. However, the PSNR of the type II network is more than 32 dB and shows about 5 dB improvement over the conventional iterative methods such as TV and Lee methods. Moreover, in spite of the difference in PSNR, the SSIM values for both methods shown in Table I are beyond the 0.97, implying that both methods can be used for clinical applications. On the other hand, the type II neural network

trained with 380 detectors, as shown in Fig. 3(b), generalizes well for all ROI sizes, including full projection data cases. Also with training data augmentation with 240, 380, 600, 1440 detectors, as shown in Fig. 3(c), there is consistent 1dB improvement for all ROI sizes. Hence, in the following experiments, the enhanced version of the type II network shown in Fig. 3(c) will be used as the type II network.

Regarding the reconstruction results by type I and type II networks for the case of 380 detector, there are non-distinguishable differences in their reconstruction profiles as shown in Figs. 6(b)(v). On the other hand, if the type I network was used for smaller ROI cases, it tends to over-estimate as shown in Fig. 6(a)(v), whereas it tends to under-estimate for larger ROI cases as shown in in Figs. 6(c-d)(v). In contrast to the type I network, the type II network provides accurate reconstruction profiles regardless of ROI sizes. This again confirms the generalization capability of the type II network.

We also compared our methods with existing iterative methods such as total variation penalized reconstruction (TV)⁶ and the L-spline based multi-scale regularization method by Lee et al⁸.

Fig. 7(i-v) shows the reconstruction results of truncated images by 380 detectors. The graphs in Fig. 7(vi) are the profiles along the white line on the each result. Fig. 7(a) shows that type I and type II networks clearly remove the cupping artifact and preserves detailed structures of underlying images. The profiles in Fig. 7(a)(vi) confirmed that the detailed structures are very well preserved by both networks. However, TV method has residual artifacts at the ROI boundaries, and the Lee method showed a drop in intensity at the ROI boundary. Fig. 7(b) shows the reconstruction results from the sagittal direction. Type I network performs slightly better than type II since the type I network is trained only with 380 detector.

Fig. 8 shows the reconstruction images from truncated 600 detectors. Type II network outperforms other methods including type I network. Type II network clearly preserves the small-scale lung nodule as well as the large-scale organs and provides the minimum NMSE values. However, type I network shows global degradation as shown in blue line of Fig. 8(vi). Similar to truncated 380 detector, the TV and Lee methods have visible artifacts at the ROI boundaries.

Table II shows the computation time. The proposed networks took about 0.05 sec/slice with GPU and 4 sec/slice with CPU, respectively. However, the TV approach in GPU took

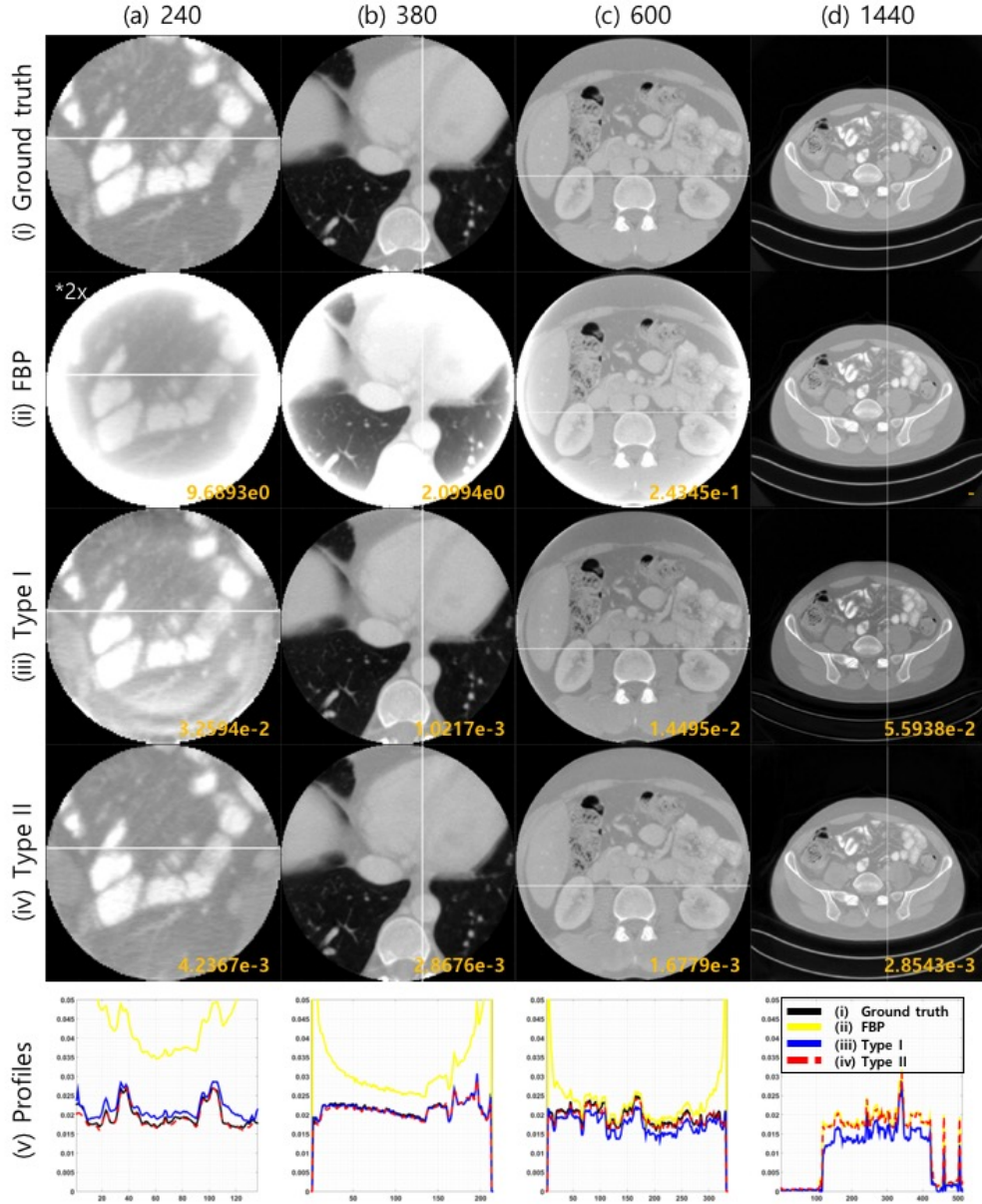
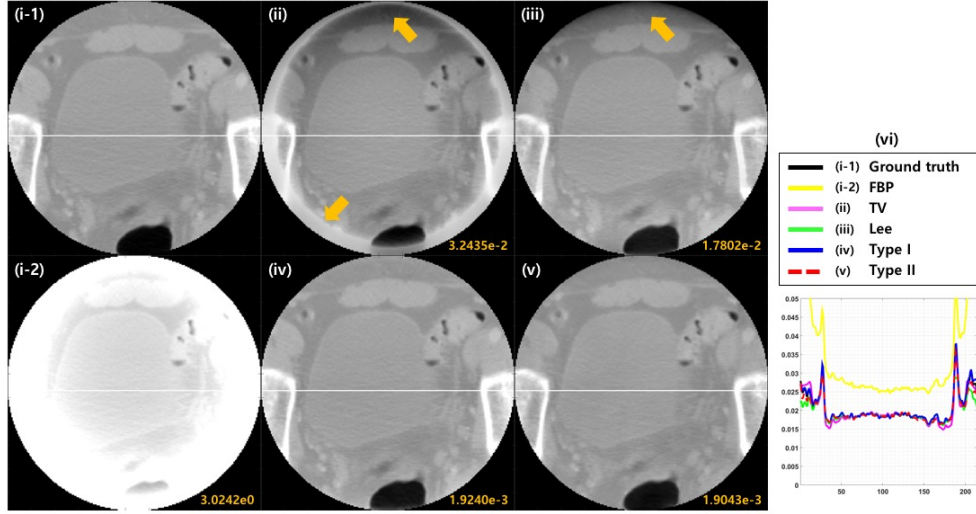
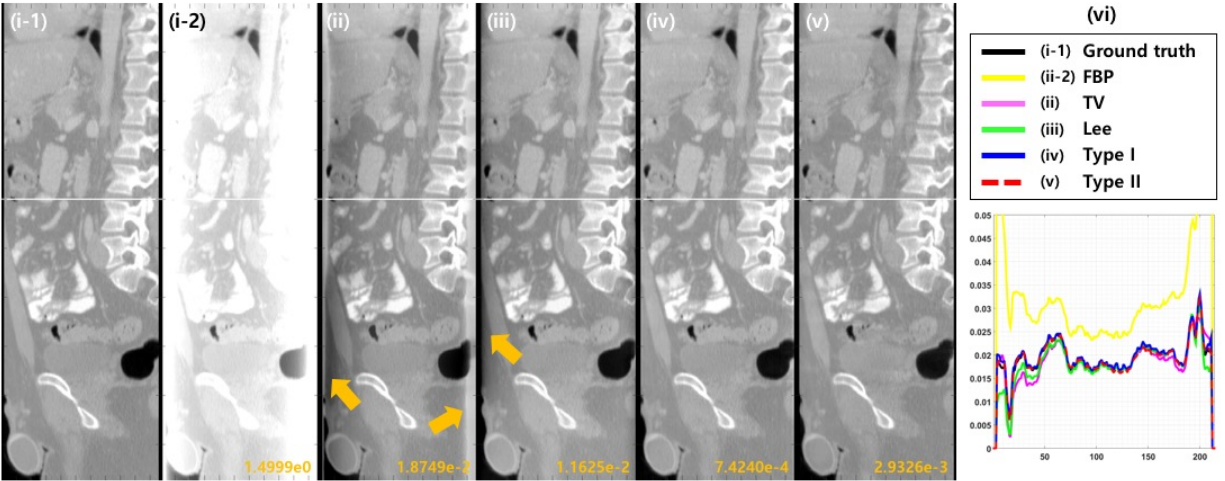


FIG. 6 Reconstruction images by (iii) type I network, and (iv) type II neural network in Fig. 3(c). (i) Ground truth and (ii) FBP images. (v) shows the profiles indicated with the white line on the results. (a-c) truncated 240, 380, and 600 detector images, and (d) full 1440 detector image. The NMSE values are written at the corner. *2x indicates that the window range is doubled.

about 11.5 sec/slice and the Lee method in CPU is about 3 ~ 9 sec/slice along the number of detector. Because the Lee method is based on a one-dimensional operation, it is faster than TV on the GPU, even though the Lee approach is implemented on the CPU. The proposed method in the GPU environment is about 60 times faster than other methods. In addition,



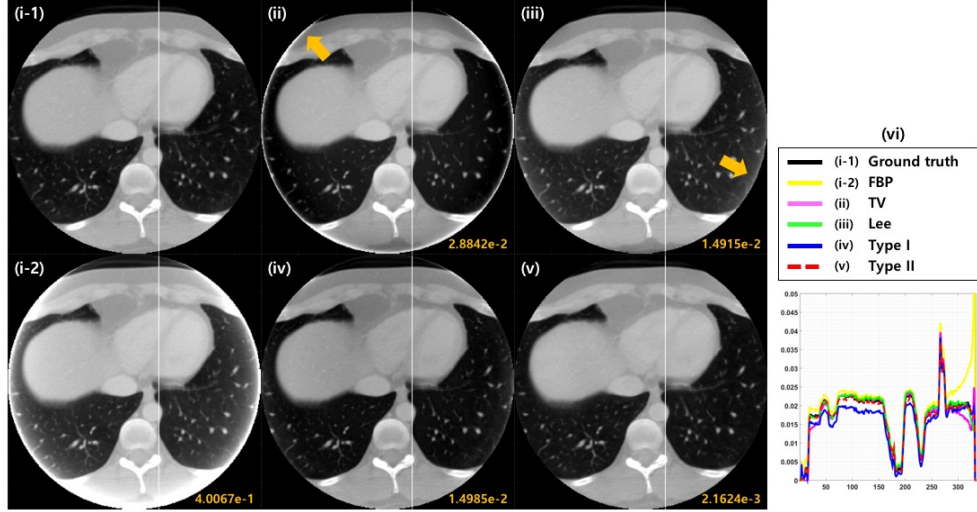
(a) Axial views of reconstruction results from truncated images by 380 detectors.



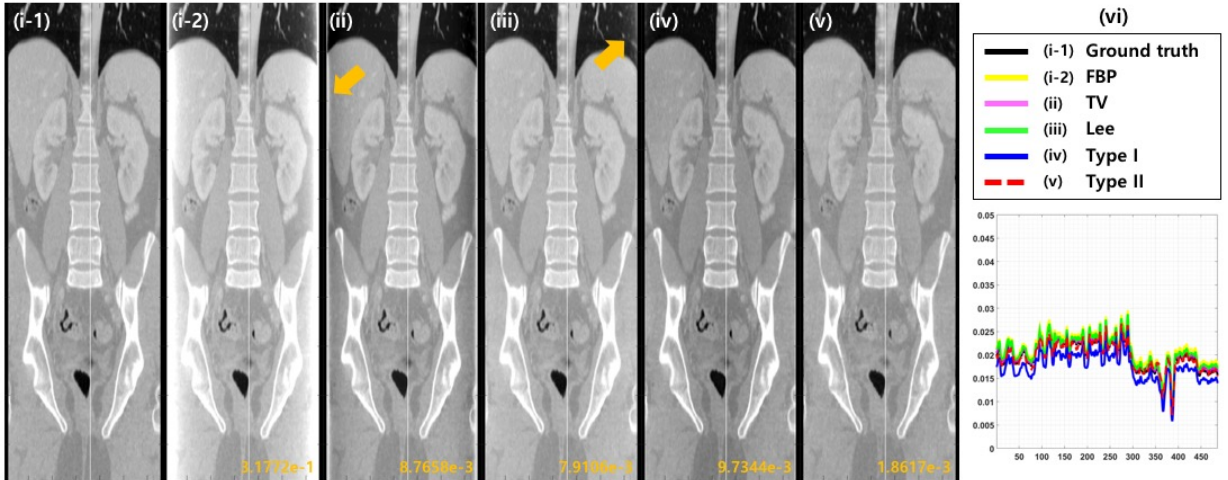
(b) Sagittal views of reconstruction results from truncated images by 380 detectors.

FIG. 7 Reconstruction images from truncated 380 detector by (ii) TV⁶, (iii) Lee method⁸, (iv) type I network¹⁸, and (v) type II network. (i-1) Ground truth, and (i-2) truncated FBP image. (vi) shows the profiles indicated with the white line on the results. The NMSE values are written at the corner.

the proposed method is 1.5 times faster on the average CPU environment. This confirms that the proposed method, regardless of the ROI sizes, shows very fast reconstruction times and provides remarkably improved image qualities compared to conventional methods.



(a) Axial views of reconstruction results from truncated images by 600 detectors.



(b) Coronal views of reconstruction results from truncated images by 600 detectors.

FIG. 8 Reconstruction images from truncated 600 detector by (ii) TV⁶, (iii) Lee method⁸, (iv) type I network¹⁸, and (v) type II network. (i-1) Ground truth, and (i-2) truncated FBP image. (vi) shows the profiles indicated with the white line on the results. The NMSE values are written at the corner.

V. CONCLUSION

In this paper, we proposed and compared two types of deep learning network for interior tomography problem. The type I network architecture is designed to learn the cupping artifacts from the analytic reconstruction, whereas the type II network architecture is to learn the inverse of the finite Hilbert transform. Due to the singularity in the artifact-

TABLE II Computation times with respect to various detector sizes.

Time [sec/slice]		TV	Lee method ⁸	Proposed	
		GPU	CPU	CPU	GPU
# of detector	240	11.6	3.3		
	380	11.7	5.1		
	600	11.9	9.3	4.0	0.05
	1440	-	-		

corrupted images, the Type I network was not well generalizable, although its performance was best at the specific ROI size used for training data. On the other hand, the input images for the Type II network are truncated DBP data that is free of singularities. Therefore, the network was shown to be well generalized for all ROI sizes. Numerical results showed that the proposed method significantly outperforms existing iterative methods in terms of quantitative and qualitative image quality as well as computation time.

ACKNOWLEDGMENT

The authors would like to thanks Dr. Cynthia McCollough, the Mayo Clinic, the American Association of Physicists in Medicine (AAPM), and grant EB01705 and EB01785 from the National Institute of Biomedical Imaging and Bioengineering for providing the Low-Dose CT Grand Challenge data set. This work is supported by National Research Foundation of Korea, Grant number NRF-2016R1A2B3008104. This work is also supported by the R&D Convergence Program of NST (National Research Council of Science & Technology) of Republic of Korea (Grant CAP-13-3-KERI).

REFERENCES

- ¹J. Hsieh, E. Chao, J. Thibault, B. Grekowicz, A. Horst, S. McOlash, and T. Myers, “Algorithm to extend reconstruction field-of-view,” in *Biomedical Imaging: Nano to Macro, 2004. IEEE International Symposium on* (IEEE, 2004) pp. 1404–1407

- ²M. Courdurier, F. Noo, M. Defrise, and H. Kudo, “Solving the interior problem of computed tomography using a priori knowledge,” *Inverse Problems* **24**, 065001 (2008)
- ³E. Katsevich, A. Katsevich, and G. Wang, “Stability of the interior problem with polynomial attenuation in the region of interest,” *Inverse Problems* **28**, 065022 (2012)
- ⁴X. Jin, A. Katsevich, H. Yu, G. Wang, L. Li, and Z. Chen, “Interior tomography with continuous singular value decomposition,” *IEEE transactions on medical imaging* **31**, 2108–2119 (2012)
- ⁵A. Katsevich and A. Tovbis, “Finite Hilbert transform with incomplete data: null-space and singular values,” *Inverse Problems* **28**, 105006 (2012)
- ⁶H. Yu and G. Wang, “Compressed sensing based interior tomography,” *Physics in Medicine and Biology* **54**, 2791 (2009)
- ⁷J. P. Ward, M. Lee, J. C. Ye, and M. Unser, “Interior tomography using 1D generalized total variation – part I: mathematical foundation,” *SIAM Journal on Imaging Sciences* **8**, 226–247 (2015)
- ⁸M. Lee, Y. Han, J. P. Ward, M. Unser, and J. C. Ye, “Interior tomography using 1d generalized total variation. part ii: Multiscale implementation,” *SIAM Journal on Imaging Sciences* **8**, 2452–2486 (2015)
- ⁹A. Krizhevsky, I. Sutskever, and G. E. Hinton, “Imagenet classification with deep convolutional neural networks,” in *Advances in neural information processing systems* (2012) pp. 1097–1105
- ¹⁰O. Ronneberger, P. Fischer, and T. Brox, “U-net: Convolutional networks for biomedical image segmentation,” in *International Conference on Medical Image Computing and Computer-Assisted Intervention* (Springer, 2015) pp. 234–241
- ¹¹E. Kang, J. Min, and J. C. Ye, “A deep convolutional neural network using directional wavelets for low-dose x-ray ct reconstruction,” *Medical physics* **44** (2017)
- ¹²H. Chen, Y. Zhang, M. K. Kalra, F. Lin, Y. Chen, P. Liao, J. Zhou, and G. Wang, “Low-dose ct with a residual encoder-decoder convolutional neural network,” *IEEE transactions on medical imaging* **36**, 2524–2535 (2017)
- ¹³Y. Han, J. Yoo, and J. C. Ye, “Deep residual learning for compressed sensing CT reconstruction via persistent homology analysis,” *arXiv preprint arXiv:1611.06391* (2016)
- ¹⁴K. H. Jin, M. T. McCann, E. Froustey, and M. Unser, “Deep convolutional neural network for inverse problems in imaging,” *IEEE Transactions on Image Processing* **26**, 4509–4522

- (2017)
- ¹⁵E. Kang, W. Chang, J. Yoo, and J. C. Ye, “Deep convolutional framelet denosing for low-dose CT via wavelet residual network,” *IEEE Transactions on Medical Imaging* **37**, 1358–1369 (2018)
- ¹⁶Y. Han and J. C. Ye, “Framing U-Net via deep convolutional framelets: Application to sparse-view CT,” *IEEE Transactions on Medical Imaging* **37**, 1418–1429 (2018)
- ¹⁷J. C. Ye, Y. Han, and E. Cha, “Deep convolutional framelets: A general deep learning framework for inverse problems,” *SIAM Journal on Imaging Sciences* **11**, 991–1048 (2018)
- ¹⁸Y. Han, J. Gu, and J. C. Ye, “Deep learning interior tomography for region-of-interest reconstruction,” in *Proceedings of The Fifth International Conference on Image Formation in X-Ray Computed Tomography* (2018)
- ¹⁹F. W. King, *Hilbert transforms*, Vol. 2 (Cambridge University Press Cambridge, UK, 2009)
- ²⁰M. Defrise, F. Noo, R. Clackdoyle, and H. Kudo, “Truncated Hilbert transform and image reconstruction from limited tomographic data,” *Inverse Problems* **22**, 1037 (2006)
- ²¹J. D. Pack and F. Noo, “Cone-beam reconstruction using 1D filtering along the projection of M-lines,” *Inverse Problems* **21**, 1105 (2005)
- ²²Y. Zou and X. Pan, “Exact image reconstruction on PI-lines from minimum data in helical cone-beam CT,” *Physics in Medicine and Biology* **49**, 941 (2004)
- ²³Y. Zou and X. Pan, “Image reconstruction on PI-lines by use of filtered backprojection in helical cone-beam CT,” *Physics in Medicine and Biology* **49**, 2717 (2004)
- ²⁴Z. Wang, A. C. Bovik, H. R. Sheikh, and E. P. Simoncelli, “Image quality assessment: from error visibility to structural similarity,” *IEEE transactions on image processing* **13**, 600–612 (2004)
- ²⁵A. Vedaldi and K. Lenc, “Matconvnet: Convolutional neural networks for matlab,” in *Proceedings of the 23rd ACM international conference on Multimedia* (ACM, 2015) pp. 689–692